coatings

MDPI

Article

Electrochemical Synthesis of a WO_3/MoS_x Heterostructured Bifunctional Catalyst for Efficient Overall Water Splitting

Ramūnas Levinas [1,2,*], Natalia Tsyntsaru [1,3], Henrikas Cesiulis [1], Roman Viter [4,5], Karlis Grundsteins [4], Loreta Tamašauskaitė-Tamašiūnaitė [2] and Eugenijus Norkus [2]

1 Faculty of Chemistry and Geosciences, Vilnius University, 03225 Vilnius, Lithuania
2 State Research Institute, Center for Physical Sciences and Technology (FTMC), 10257 Vilnius, Lithuania
3 Institute of Applied Physics, Moldova State University, 2028 Chisinau, Moldova
4 Institute of Atomic Physics and Spectroscopy, University of Latvia, 1586 Riga, Latvia
5 Center for Collective Use of Scientific Equipment, Sumy State University, 40018 Sumy, Ukraine
* Correspondence: ramunas.levinas@chf.vu.lt

Abstract: Photo-/electrochemical water splitting can be a suitable method to produce "green" hydrogen and oxygen by utilizing renewable energy or even direct sunlight. In order to carry out photoelectrochemical (PEC) water splitting, a photoanode based on transition metal oxides, which absorbs photons and produces photoexcited electron–hole pairs, is needed. The positively charged holes can then participate in the water oxidation reaction. Meanwhile, a cathodic hydrogen evolution reaction (HER) can occur more efficiently with electrocatalytic materials that enhance the adsorption of H^+, such as MoS_2. In this study, it was shown that WO_3/MoS_x heterostructured materials can be synthesized by an electrochemical method called plasma electrolytic oxidation (PEO). During this process, many micro-breakdowns of the oxide layer occur, causing ionization of the oxide and electrolyte. The ionized mixture then cools and solidifies, resulting in crystalline WO_3 with incorporated MoS_x. The surface and cross-sectional morphology were characterized by SEM-FIB, and the coatings could reach up to 3.48 µm thickness. Inclusion of MoS_x was confirmed by EDX as well as XPS. Synthesis conditions were found to have an influence on the band gap, with the lowest value being 2.38 eV. Scanning electrochemical microscopy was used to map the local HER activity and correlate the activity hotspots to MoS_x's content and surface topography. The bifunctional catalyst based on a WO_3/MoS_x heterostructure was evaluated for PEC and HER water-splitting activities. As a photoanode, it could reach up to 6% photon conversion efficiency. For HER in acidic media, a Tafel slope of 42.6 mV·dec^{-1} can be reached.

Keywords: plasma electrolytic oxidation; tungsten oxide; molybdenum sulfide; heterostructure; water splitting; electrocatalysis; hydrogen evolution reaction; photoanode; scanning electrochemical microscopy

check for updates

Citation: Levinas, R.; Tsyntsaru, N.; Cesiulis, H.; Viter, R.; Grundsteins, K.; Tamašauskaitė-Tamašiūnaitė, L.; Norkus, E. Electrochemical Synthesis of a WO_3/MoS_x Heterostructured Bifunctional Catalyst for Efficient Overall Water Splitting. *Coatings* **2023**, *13*, 673. https://doi.org/10.3390/coatings13040673

Academic Editor: Ming-Tzer Lin

Received: 28 February 2023
Revised: 21 March 2023
Accepted: 23 March 2023
Published: 25 March 2023

1. Introduction

In the near future, in order to drive certain industrial and technological processes, utilization of solar energy will become more widespread than ever. This is proven by economic outlook reports such as that issued by the International Energy Agency, Renewables 2022, which forecasts global solar photovoltaic capacity to triple over the period 2022–2027. Furthermore, solar energy is actively being investigated as a viable solution for such issues as CO_2 reduction and water splitting to produce hydrogen [1,2]. Hydrogen in particular is a promising fuel for the future as it has the largest gravimetric current density of all known substances (~120 kJ·g^{-1}) [3], and therefore could be used to power energy-intensive technologies. Admittedly, the use of liquid hydrogen as an energy carrier faces many fundamental problems, one of which is its production.

Nowadays, the production of hydrogen cannot be separated from the strive for climate neutrality. Although hydrogen can be produced in large quantities by steam methane

reformation, it is classified as grey hydrogen due to the large carbon footprint of this process; this is in contrast to green hydrogen, which is synthesized using only renewable sources [4]. However, green hydrogen production processes (such as photoelectrochemical water splitting/electrolysis) are much less effective, thus the resulting hydrogen is more expensive and, as of yet, uneconomical [5].

The efficiency of solar light utilization in photoelectrochemical (PEC) processes is directly related to the band gap of the light absorbing material. The thermodynamic limit for the onset of water splitting is 1.23 eV, and the catalytic material should have a band gap close to this value. In reality, this is hardly achievable, but some transition metal oxides have a combination of properties that make them prime candidates for PEC catalysis. WO_3 is one of these materials, as it has a band gap of ~2.7 eV, which can be further lowered by tuning the synthesis conditions or creating heterostructures with other materials [6–8]. In addition, WO_3 is relatively stable under anodic conditions in acidic media, though it does undergo noticeable photo-corrosion in different electrolytes [9]. Photoactive WO_3 films have been prepared through various methods such as hydrothermal [10,11] or sol-gel synthesis [12], magnetron sputtering [13], spray/aerosol pyrolysis [14,15], as well as electrochemically on the cathode [16–18] or anode [19,20]. A modification of anodic synthesis is plasma electrolytic oxidation (PEO), which has been used to grow transition metal oxide coatings and heterostructures [21–23].

Another material that is often used for electrochemical water splitting is molybdenum sulfide (MoS_2) [24]. It is used as an electrocatalyst for hydrogen evolution reaction (HER)s in acidic media because of the favorable thermodynamics of H^+ adsorption on the surface active sites [25]. The mechanism of HER on MoS_2 is identical to that on Pt. Thus, MoS_2 can be considered a non-precious metal electrocatalyst and an alternative to Pt [26]. It is also a semiconductor with a tunable band gap, averaging ~1.7 eV for 2H-MoS_2 [27]. MoS_2 has also been used in bifunctional catalysts to improve the HER activity of an oxygen evolution reaction (OER) catalyst [28]. Various methods have been developed to synthesize photoactive MoS_2 structures [29], the more prominent being chemical vapor deposition (CVD) [30–32], wet chemical synthesis [33,34], and electrochemical deposition [35–38].

New materials based on WO_3 and MoS_2 have been synthesized by methods such as sol-gel spin coating, probe sonication, or wet chemical synthesis, and were tested for electrochromic devices [39], as sensors [40] and photocatalysts [41].

In this study, the possibility of depositing WO_3 and MoS_2 through a one-stage process, namely PEO, is investigated. Although this method has been known for decades, it is regaining attention in the scientific community [42,43]. PEO is an excellent method to produce transition metal oxide films with unique properties. It also provides the possibility to incorporate ions into the film. Therefore, a new bifunctional WO_3/MoS_x heterostructured catalyst was synthesized and comprehensively evaluated. The perspectives of this novel heterostructure, in which WO_3 can act as a photoanode and the MoS_2 as a lower band gap semiconductor, and the HER electrocatalyst were also assessed.

2. Materials and Methods

2.1. Plasma Electrolytic Oxidation Procedure

Tungsten plates (99.5%, Alfa Aesar, Ward Hill, MA, USA) were used as working electrodes with a geometrical area of 2 cm^2. They were connected as the anode in a two-electrode cell, with a stainless steel coil as the counter electrode. The WO_3/MoS_x heterostructures were obtained from the following electrolytes: 1 M Na_2SO_4 (≥99%, Roth, Karlsruhe, Germany), 75 mM NaF (≥99%, Roth), 0.1 M NaH_2PO_2 (≥99%, Roth), and 25 mM of MoS_4^{2-}. The last component was synthesized from $(NH_4)_6Mo_7O_{24}{\cdot}4H_2O$ (≥99%, Roth) and 60% Na_2S (Roth). WO_3 films were also obtained from the same bath, but without MoS_4^{2-} for comparison. The syntheses were carried out at room temperature (22 ± 3 °C) under galvanostatic conditions (Consort EV245, Cleaver Scientific, Rugby, Warwickshire, UK) power supply) by applying current of 50 mA. The solution was agitated with a magnetic stirrer. In order to evaluate the influence of the targeted properties, the duration

of synthesis was 2, 5 and 30 min. The tags 2-min, 5-min, and 30-min WO_3 or WO_3/MoS_x were assigned, respectively.

2.2. Structural Characterization

An FEI Helios Nanolab 650 (Hillsboro, OR, USA) dual beam system with an energy dispersive X-ray (EDX) spectrometer INCA Energy 350 (Oxford Instruments, Abingdon, Oxfordshire, UK) and X-Max 20 mm^2 (Oxford Instruments, Abingdon, Oxfordshire, UK) detector was used to observe the surface morphology by scanning electron microscopy and EDX mapping. A Ga^+ ion beam was used for focused ion beam (FIB) analysis. The XPS analyses were carried out with a Kratos Axis Supra spectrometer (Kratos Analytical Limited, Manchester, UK) using a monochromatic Al K(alpha) source (25 mA, 15 kV). Survey scan analyses were carried out on the area of 300 µm × 700 µm at a pass energy of 160 eV. High-resolution analyses were carried out also on the area of 300 µm × 700 µm, but at a pass energy of 20 eV. The XPS signal due to adventitious carbon located at 284.8 eV was used as a binding energy (BE) reference. An X-ray diffractometer (D2 Phaser, Bruker, Billerica, MA, USA, λ = 1.5418 Å/Cu Kα) was used to characterize the crystal structure of the obtained films.

2.3. Optical Properties

Diffuse reflectance spectra were measured in the range of 250–900 nm by means of an Ocean Optics HR4000 spectrometer (Ocean Insight, Orlando, FL, USA), Ocean Optics reflectance probe (angle 45°) and deuterium–halogen light source (DH-2000-BAL, Ocean Insight, Orlando, FL, USA). Diffuse reflectance R was converted to absorbance F using the following known Kubelka–Munc equation:

$$F = \frac{(1-R)^2}{2 \cdot R} \tag{1}$$

Band gap E_g was graphically calculated from the following equation:

$$(F \cdot hv)^{1/2} = A\left(hv - E_g\right) \tag{2}$$

2.4. Photo-/Electrochemical Characterization and Electrochemical Treatment

All photo- and electrochemical measurements were carried out by means of an Autolab 302 N (Metrohm, Utrecht, The Netherlands) potentiostat connected to an Autolab optical bench system. A 365 nm LED (Thorlabs, Newton, NJ, USA) was used for photoexcitation, with the light intensity calibrated to 25 mW cm^{-2}. The photoelectrochemical (PEC) properties of synthesized films were evaluated in a quartz three-electrode cell with a Ag/AgCl reference electrode and a stainless steel counter electrode. The HER characterization was carried out in a regular 3-electrode glass cell. An electrochemical reduction-activation treatment was carried out to prove the possibility of further improving the PEC properties of the heterostructures. Specific experimental steps are summarized in Table 1, and have been described in detail recently [44,45]. The potential values were recalculated vs. RHE, and are presented as such throughout the study, unless it is stated otherwise.

The relationship between incident light intensity (I_0) and photon conversion efficiency was also evaluated by measuring potentiostatic light pulses at 1.53 V, but under different I_0, from 5 mW cm^{-2} to 30 mW cm^{-2}. Obtained photocurrent values were recalculated to incident photon conversion efficiencies (*IPCE*) by Equation (3):

$$IPCE\ (\%) = \frac{j_{ph}\left(\text{mA cm}^{-2}\right) \times 1240(\text{V nm})}{I_0(\text{mW cm}^{-2}) \times \lambda(\text{nm})} \tag{3}$$

Table 1. Outline of experiments used to characterize the PEC and HER properties of synthesized catalysts. Potentials were recalculated vs. RHE.

Step	PEC (0.1 M Na_2SO_4, pH 2)	HER (0.5 M H_2SO_4)
1	Settling of OCP for 60 s.	Settling of OCP for 60 s.
2	LSV scan from 0.72 V to 2.3 V at 2 mV·s^{-1}, with 10 s ON/OFF pulses of 25 mW·cm^{-2} 365 nm light.	LSV at 2mV·s^{-1} from 0 V to a cut-off current density −100 mA·cm^{-2}.
3	Potentiostatic illumination pulse at 1.53 V.	EIS measurements from −0.1 V to −0.5 V. Spectra obtained from 10 kHz to 100 mHz, perturbation amplitude ±10 mV.
4	Electrochemical reductive treatment of 30-min-WO_3/MoS_x	Fitting data with Zview software.
5	Repeat of steps 1–3 for r-30-min-WO_3/MoS_x	

2.5. Scanning Electrochemical Microscopy (SECM)

SECM measurements were carried out using a Versa SCAN (Ametek, Berwyn, PA, USA) workstation connected with Versta STAT 3 and Versa STAT 3F bipotentiostat setup (Princeton Applied Research, Oak Ridge, TN, USA). The mode of operation was substrate generation/tip collection (SG/TC), wherein the substrate (WO_3/MoS_x heterostructures) was a generator, and the tip (25 µm Pt) was a collector. The substrate was immersed in 0.5 M H_2SO_4 solution. Before measurement, the substrates were subjected to an equilibration treatment by applying a −0.3 mA·cm^{-2} current for 20 min until a stable overpotential related to HER is reached. After suitable conditions were reached, the probe was lowered to ~15–25 µm of the substrate by a typical approach curve method. Then, the probe was polarized to 0 V (vs. Ag/AgCl), which had been determined to give a good hydrogen oxidation signal, and a 2D map was obtained by scanning the probe at a speed of 100 µm s^{-1} and measuring data points at 25 µm increments.

3. Results and Discussion

3.1. Synthesis and Structural Characterization of Heterostructures

PEO can be characterized by measuring the change of voltage with time under galvanostatic conditions. Similarly to TiO_2 [46,47], the WO_3 formation process (Figure 1) undergoes three consecutive stages. At the beginning of oxidation, voltage increases almost linearly with time, and the conventional anodic oxidation of W occurs. The growth of the anodic WO_3 can be represented by the three-step process (Equations (4)–(6)), wherein metallic W is electrochemically dissolved and interacts with water from the solution to form WO_3 film [48]:

$$W + 2H_2O \rightarrow WO_2^{2+} + 4H^+ + 6e^- \quad (4)$$

$$WO_2^{2+} + 2H_2O \rightarrow W_2O_5 + 2H^+ \quad (5)$$

$$W_2O_5 + H_2O \rightarrow 2WO_3 + 2H^+ + 2e^- \quad (6)$$

In this stage, the voltage increases rapidly to maintain the applied current as the oxide layer grows, although some current is consumed for oxygen gas evolution. Notably, the obtained slopes of the V-t curves are very steep for both WO_3 and WO_3/MoS_x, and the value of ~65 V is reached within 0.5 s (~130 V s^{-1}). For comparison, the slopes observed for TiO_2 in various electrolytes were 24 to 35 V s^{-1} [47]. It has been proposed that the voltage at the end of stage I is called the "breakdown voltage" (V_b), which in this case is

approximately 65 V for both WO_3 and the heterostructure. This is much lower than that for TiO_2, but it is expected because WO_3 is a less dielectric material.

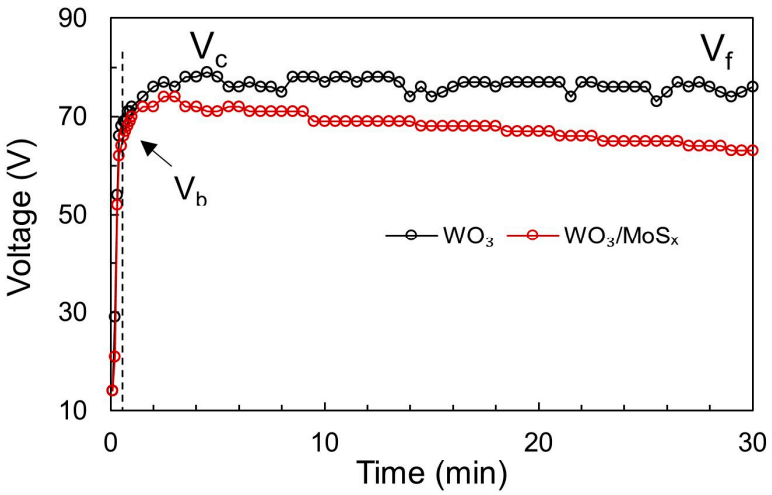

Figure 1. Voltage vs. time plots obtained for PEO of W at 25 mA cm^{-2} during synthesis of WO_3 and WO_3/MoS_x heterostructures in the respective electrolytes.

When V_b is reached, the second oxidation stage begins, in which the slope of V-t decreases and tiny electric sparks generate the micro-breakdowns in the film. Now, the total current is governed by two components: the ionic current and the electric current. Due to this reason, a lower voltage is needed to maintain the applied current. The voltage may still increase until V_c (critical voltage), where V_c = 79 V for WO_3 and V_c = 74 V for the WO_3/MoS_x heterostructure.

In stage III, the voltage values are almost constant and approach the final voltage (V_f). This is the case for WO_3, and it means that the film has attained a constant resistance. However, for WO_3/MoS_x, the voltage drops from a maximum V_c = 74 V to V_f = 63 V. Because a lower voltage is needed to maintain the applied current, the films become more conductive when MoS_2 is incorporated. Notably, ions from the electrolyte can be incorporated into the film during PEO because of complex chemical, electrochemical, and physical processes that occur during this process [49]. To generalize, electron avalanches during micro-breakdowns ionize both the oxide and electrolyte, and a mixture is formed and then solidifies again. However, in this particular case of MoS_2, the anodic formation of MoS_3 can also occur by disproportionation of MoS_4^{2-} [50,51], by reaction 7, as proposed in [52]:

$$MoS_4^{2-} \rightarrow MoS_3 + \frac{1}{8}S_8 + 2e^- \quad (7)$$

For further characterization, the heterostructured films were synthesized by capping PEO time to match the different stages: 2 min to reach V_b, 5 min when V_b is passed and value of V_c is reached, and 30 min for V_f. The surface and bulk morphologies of the obtained materials are shown in Figure 2, and are similar to those obtained for the plain WO_3 that had been formed by a similar method [45] The films synthesized for 2 and 5 min are disorderedly nanoporous, with surface pore diameters apparently ranging up to several hundred nanometers (Figure 2a,b). Such pores are also sometimes called "discharge channels". In addition, it is evident from the cross-sections of the respective samples (Figure 2d,e) that the channels do not propagate vertically from the substrate, as would be expected in a typical anodic tungsten oxide structure. On the contrary, the cavities within the growing material seem to preferentially propagate horizontally. This is the result of the PEO mechanism of oxide layer growth. At certain locations, film breakdown occurs and the electron avalanche flowing between the metallic W substrate and the film–electrolyte interface ionizes the oxide with some amount of electrolyte and causes a vapor blowout, leaving behind a cavity and ionized plasma mixture. The plasma is then cooled by the

electrolyte, hardening and forming a pore. It is also worth distinguishing the film, obtained after 30 min (Figure 2c,f), the morphology of which is much rougher, although it was shaped by the same fundamental processes, only for a much longer duration. The average thickness of the films is linearly dependent on synthesis time, and ranges from 0.56 µm (±0.13 µm) to 3.48 µm (±1.1 µm) as the synthesis duration is increased from 2 to 30 min.

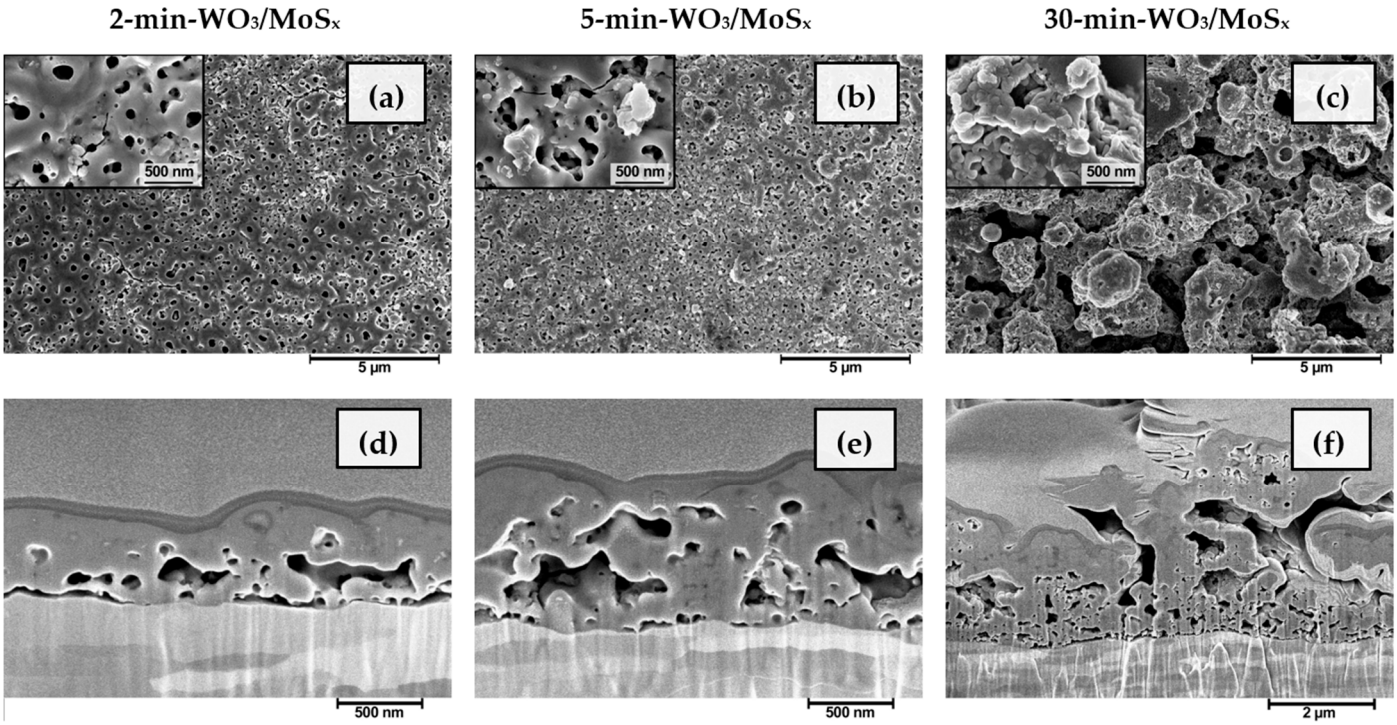

Figure 2. SEM surface morphology and FIB cross-sectional morphology of WO_3/MoS_x heterostructures, obtained after synthesis for 2 min (**a**,**d**), 5 min (**b**,**e**), 30 min (**c**,**f**).

The crystalline nature of the films was revealed by XRD. Typically, non-annealed WO_3 films that had been obtained by anodization are amorphous [53], but in this case, the diffractograms show that the peaks correspond to a monoclinic WO_3 structure, wherein the (002), (020), and (200) peak intensities have similar proportions for all coatings (Figure 3). The relative intensities of monoclinic WO_3 peaks are larger for thicker films, and distinct W substrate peaks are also detected for all samples. This is due to the X-ray penetration depth, because a stronger substrate signal and weaker oxide signal are seen for thinner films. All of the films, regardless of synthesis time, have a monoclinic structure. This is yet another effect of the PEO mechanism of oxide film growth; although no external heat is applied, the plasma caused by electric discharges produces enough energy to electrodeposit a crystalline material. Small peaks at the 2θ range of 50° to 60° that could not be attributed to WO_3 appear on the diffractogram of the thickest film. Peaks at such 2θ values have been observed for hexagonal and synthesized MoS_2 [54,55]. The weak signal is most likely related to the small amount of incorporated MoS_x and the amorphous-like structure of it.

In the structural characterization of these heterostructured materials, it is important to investigate how MoS_2 is dispersed throughout the WO_3 matrix. For this purpose, the films of a WO_3/MoS_x sample deposited for 30 min were examined by an EDX mapping technique, which was carried out for areas on an FIB channel cross-section (Figure 4a) and top-down surface (Figure 4b). A strong tungsten signal was obtained, and the quantity of W correlates with O, suggesting the existence of a tungsten trioxide. The presence of Mo and S was also confirmed, but the excitation energies for these materials overlap in EDX analysis, so no definite quantitative conclusions could be drawn. However, the maps show that the MoS_2 material is detected on the surface of the electrode in larger chunks of

micrometer-order diameters. Cross-sectional EDX maps were also obtained for the thinner films (synthesized for 2 and 5 min), but no discernible Mo or S signal could be obtained.

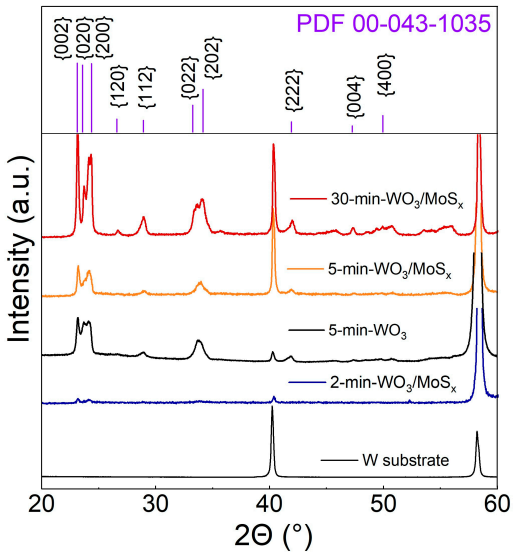

Figure 3. XRD diffractograms of W substrate, a WO_3 film synthesized for 5 min, and heterostructured films, synthesized for 2, 5, and 30 min.

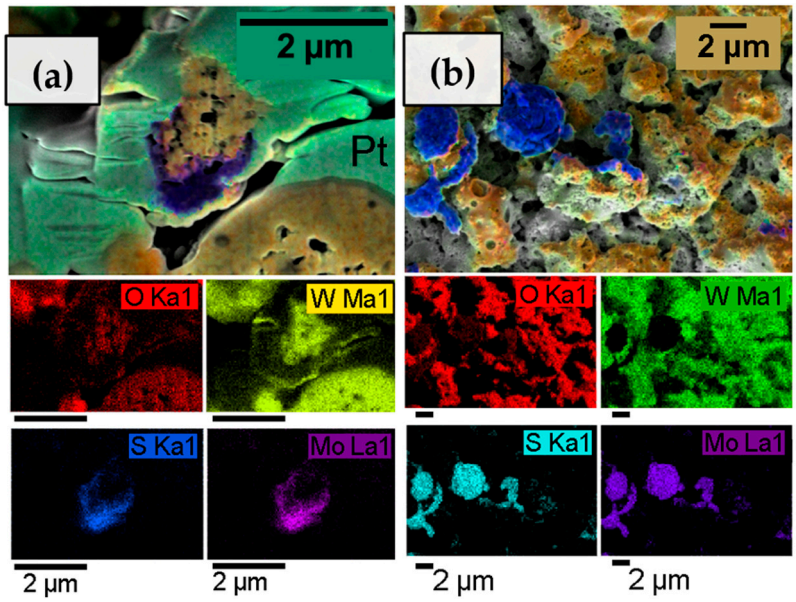

Figure 4. EDX elemental composition maps of 30-min-WO_3/MoS_x heterostructured coating. Cross-sectional view (**a**), and top-down view (**b**).

Although the signal of Mo and S was not always strong enough for mapping, EDX data obtained for top-down areas of the samples show that Mo, S, and P are detected in the film. Up to ~1.5 % of P is detected in the films, and the amount does not vary with deposition time. P is incorporated into the film from $H_2PO_2^-$, as plasma discharges ionize the oxide and electrolyte and later cool down to a solid material. As for Mo and S, both materials are detected in the elemental composition of the films, but not in any expected stoichiometries such as MoS_2 or MoS_3. In fact, the apparent composition of MoS_x is severely sulfur-deficient (e.g., $MoS_{0.4}$ for 5-min-WO_3/MoS_x). This probably occurs due to molybdenum sulfide oxidation to some degree under anodic deposition conditions.

XPS was used to check whether the MoS_x material is in fact comprised from Mo-S bonds. The core-level Mo3d XPS spectrum (Figure 5a) displayed the same characteristic

peaks that had been observed for MoS_2 synthesized by other methods [56,57], particularly for cathodically electrodeposited MoS_2 [44]. The Mo3d region deconvolutes into several doublets that are related to Mo^{6+}-O bonds ($3d_{5/2}$ 232.7 eV; $3d_{3/2}$ 235.7 eV), Mo^{4+}-S bonds ($3d_{5/2}$ 229.3 eV; $3d_{3/2}$ 232.1 eV), and a Mo^{5+} signal, which may be related to a heptavalent oxide, but also to sulfur-deficient Mo/active sites ($3d_{5/2}$ 230.9 eV; $3d_{3/2}$ 234.2 eV). Interestingly, the S2p core-level spectra (Figure 5b) deconvolute into two clear doublets, the existence of which can be attributed to terminal (S-term. $S2p_{3/2}$ 161.8 eV; $Sp_{1/2}$ 163.0 eV) and bridging (S-br. $S2p_{3/2}$ 163.2 eV; $S2p_{1/2}$ 164.2 eV) S bonds within the material [56]. Unlike for cathodically deposited MoS_2, a very strong signal of the bridging sulfide bond component is seen. This observation implies a somewhat different structure in the MoS_x deposited anodically. Similar behaviors were reported in the literature [58]. This also may have a pronounced effect on the material's use as an HER electrocatalyst; terminal sulfur bonds may break during hydrogen evolution, leaving a sulfur-deficient Mo/an active site. A molybdenum sulfide structure comprising mostly bridging bonds may be less susceptible to corrosion, but is also less electrocatalytically active. The W4f core-level spectra of this film showed that the material is almost entirely W^{6+} oxide (99.52%), with a very small W^{5+} signal (0.48%) (Figure 5c).

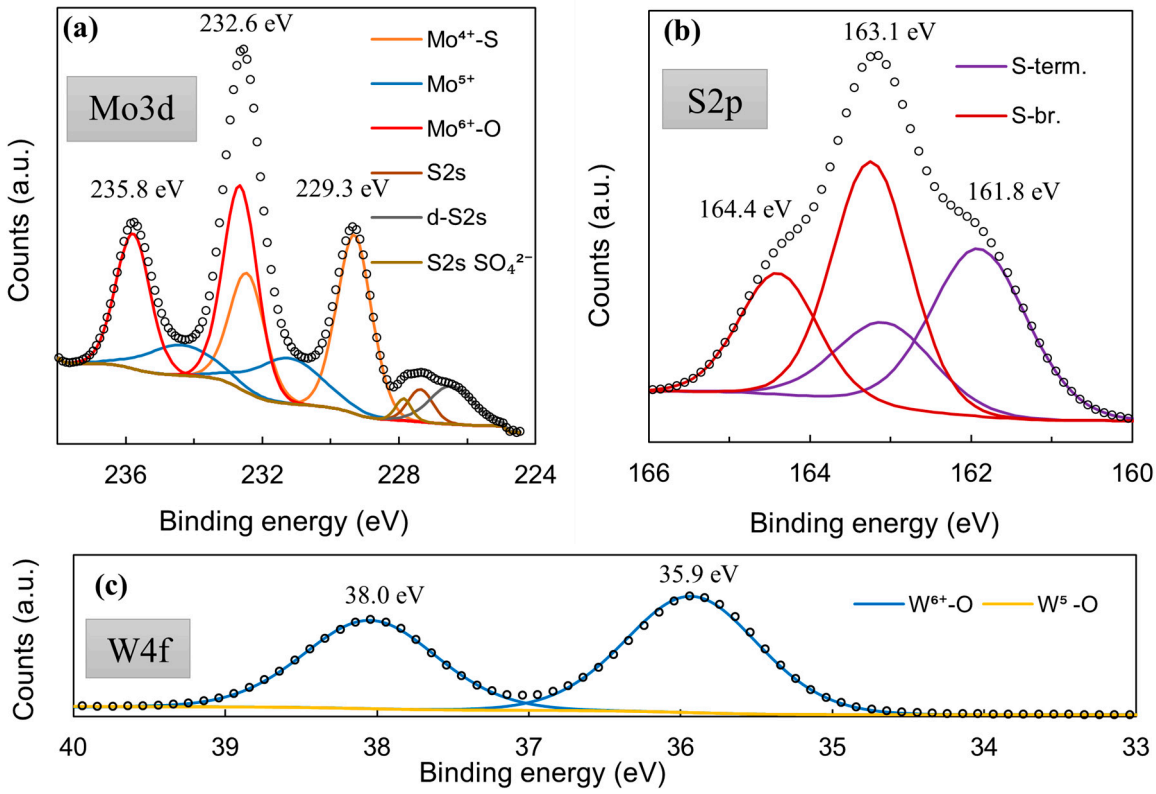

Figure 5. High-resolution XPS spectra of a 5-min-WO_3/MoS_x film: Mo3d (**a**), S2p (**b**), W4f (**c**).

3.2. Properties of WO_3/MoS_x Heterostructures

3.2.1. Optical Properties

The optical properties of the heterostructured and WO_3 films were measured by UV-visible light spectroscopy. Figure 6a shows the diffuse reflectance spectra obtained at wavelengths in the range of 300 to 800 nm. As expected, the absorption maximum for all films lies in the UVA range at ~360 nm. Moreover, the heterostructures have evidently decreased reflectance in comparison to 5-min-WO_3 film, which attests to the changes in the structure of the obtained novel materials. Furthermore, an increase in the synthesis time resulted in a red shift of the absorption edge. These films also have a fairly prominent absorption tail in the visible light region. It has been proposed that for WO_3-based materials, visible light absorption can be attributed to surface W^{5+} sites [59,60]; however, in this study,

XPS showed almost no W^{5+} for 5-min-WO_3/MoS_x. Thus, visible light absorption may be an effect of compositing with MoS_x, or perhaps the existence of W^{5+} sites deeper within the film cavities into which XPS cannot penetrate. The band gaps also depend on synthesis conditions and have a clear tendency to decrease with increased synthesis time (Figure 6b). In particular, 2.75 eV, 2.49 eV, and 2.38 eV band gaps were calculated for the 2-min, 5-min, and 30 min films, respectively. The 5-min-WO_3 has a larger band gap (2.66 eV) than the heterostructure counterpart, which indicates alteration of optical properties through incorporation of MoS_x.

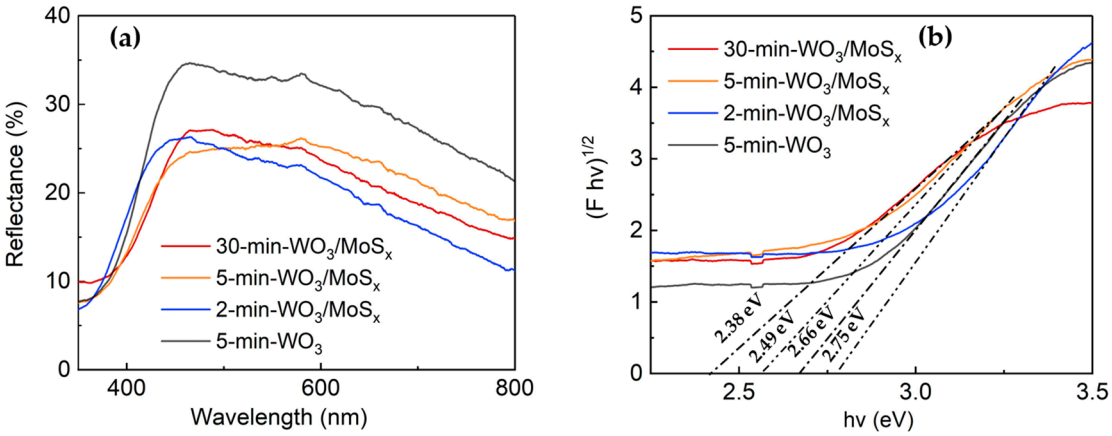

Figure 6. Diffuse reflectance spectra (**a**) and Tauc plots with band gap calculations (**b**) of WO_3/MoS_x and 5-min-WO_3 films.

3.2.2. Photoelectrochemical Properties

The PEC activity curves obtained for WO_3 and WO_3/MoS_x films are shown in Figure 7a,c,e. For all films, starting from onset at ~0.8 V, the photocurrent increases with applied potential, which is expected as the space–charge layer expands. The photocurrent of the films that had been synthesized for 2 min is relatively similar, which may be explained by recalling Figure 1 and the related discussion. During this shortest duration of synthesis, the same voltage is reached, regardless of the presence of MoS_4^{2-} in the electrolyte. Consequently, very little MoS_x is incorporated into the film. For the 5 min WO_3 and WO_3/MoS_x films, an essential difference in their PEC properties is seen, illustrating the effect of incorporation of MoS_x into WO_3. The thickest films are unique; 30-min-WO_3 has very poor PEC activity, whereas the heterostructure shows significantly higher activity. The 30-min-WO_3/MoS_x film has a strong anodic background current component that can be inferred from the "UV OFF" parts of the LSV curve. The origin of such current is electrochemical rather photoelectrochemical, and may be related to the charging current of a large surface area. However, anodic oxidation of the incorporated MoS_x material is also possible.

Potentiostatic light pulse measurements were carried out in order to evaluate the steady-state photocurrent, and the data obtained at 1.53 V vs. RHE are presented in Figure 7b,d,f. The largest photocurrent is generated by the 5-min-WO_3/MoS_x sample is ~0.47 mA·cm^{-2}, representing a 2.6-fold improvement over 0.17 mA·cm^{-2} for 5-min-WO_3. Here, it is also important to examine the initial photocurrent ($j_{t=0}$) versus the steady-state photocurrent, which is assumed as the stable current at the end of the 30 s pulse ($j_{t=30}$) minus the background current ($j_{ph} = j_{t=30} - j_{bg}$). If $j_{t=0}$ is larger than $j_{t=30}$, we know that recombination of photogenerated holes and electrons occurs at the electrode–electrolyte interface, and this limits the photoelectrochemical current. In this case, no significant recombination is seen. In addition, for the 30-min-WO_3/MoS_x, sample $j_{t=0}$ is smaller than $j_{t=30}$, which shows slower photogenerated charge transfer kinetics.

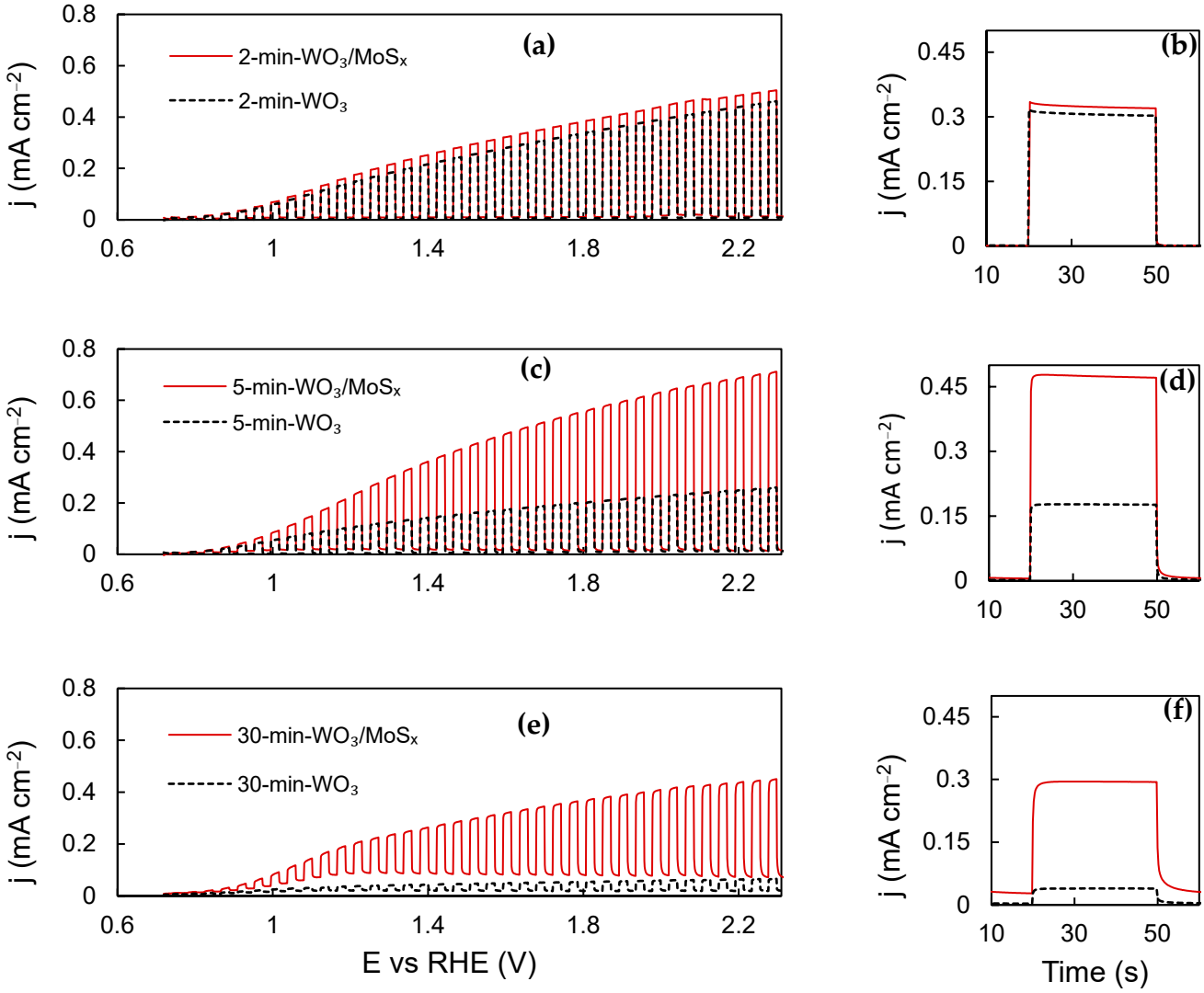

Figure 7. Chopped-UV LSV curves (**a**,**c**,**e**) and steady-state photocurrent pulses, measured at 1.53 V (**b**,**d**,**f**). See Table 1 for more details.

Previously, it was demonstrated that cathodic electrochemical reduction/H^+ intercalation into WO_3 films synthesized by the same method enhances their PEC properties [45]. This is also true for obtained WO_3/MoS_x heterostructures, and the biggest improvement in PEC properties was obtained for the thickest film (30-min-WO_3/MoS_x). The chronoamperometric curve registered during reduction shows that the current density settles at ~−4 mA·cm^{-2}, compared to −0.3 mA·cm^{-2} for a plain WO_3 film (Figure 8a). Then, a potential of 1.53 V was applied and the electrode was illuminated, with 2 s OFF pauses every 60 s. (Figure 8b). The photocurrent, which is the difference between the dark current and total current, plateaus after ~2000 s. Then, the PEC characterization was repeated, and it is evident that the reduced film (r-30-min-WO_3/MoS_x) exhibits superior performance to the entire measured potential range (Figure 8c) and in steady-state pulse measurements (Figure 8d), estimated to be an increase of ~30%. This improvement can be attributed to the same process that had been characterized with XPS before, i.e., the reduction of W^{6+} to W^{5+} by intercalated protons, followed by oxygen vacancy restructuring towards more optimal levels during activation [45].

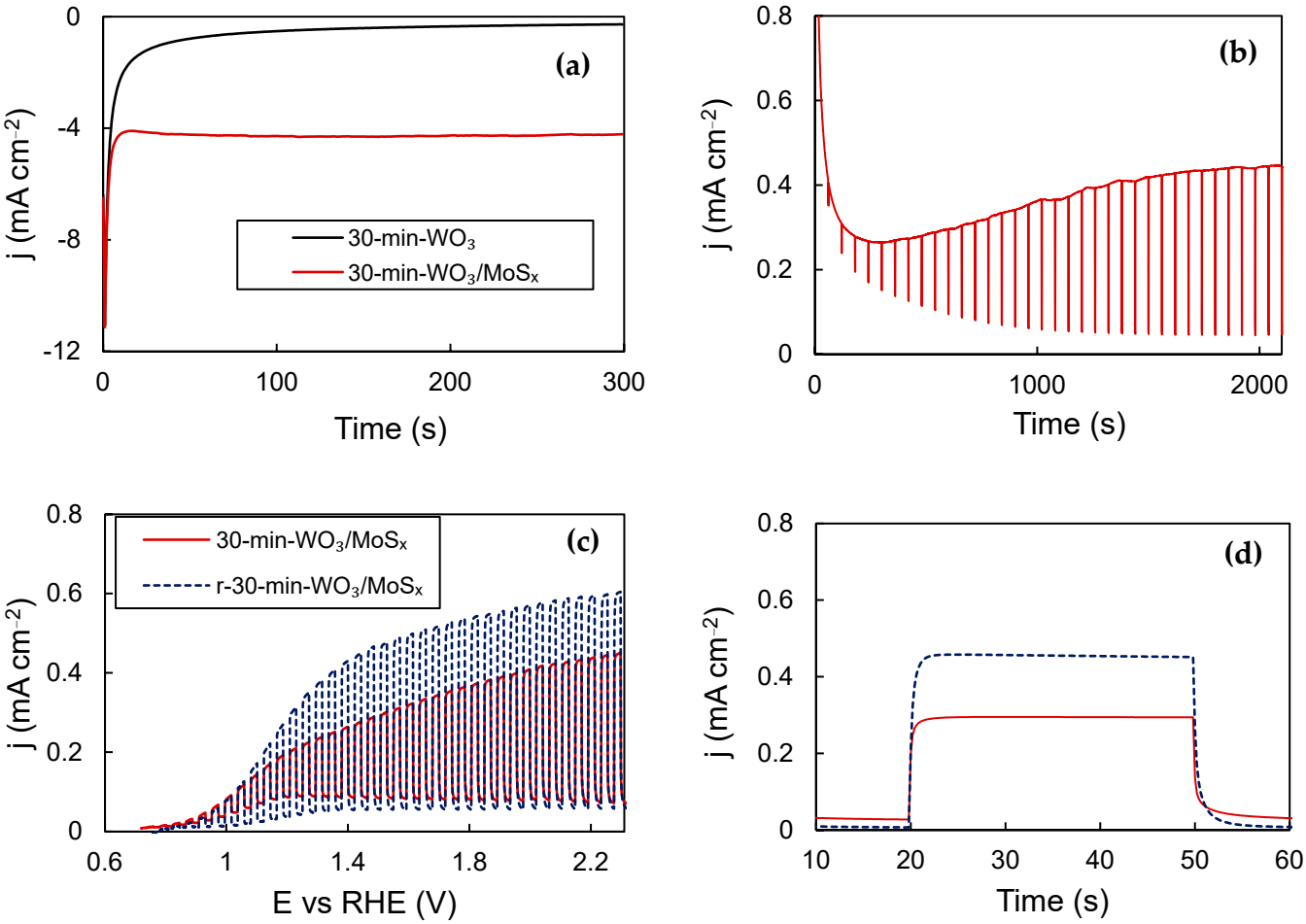

Figure 8. Chronoamperometric curves for WO_3/MoS_x and WO_3 reduction at −0.28 V (**a**); activation curve of reduced 30-min-WO_3/MoS_x (**b**); chopped-UV LSV curves (**c**); steady-state photocurrent pulses (**d**). See Table 1 for more details.

In order to establish a more comprehensive characterization of the PEC properties of these materials, the photocurrent response was evaluated in relation to the light intensity (I_0). According to the simplified Gärtner–Butler equation [61], the current generated by a photoanode will be a function of two variables: the width of the space charge layer and incident photon flux. The former is related to applied/bias potential and is reflected by potential sweep experiments, whereas the incident photon flux is directly proportional to I_0. As can be inferred from the Gärtner–Butler equation, provided charge carrier photogeneration and transfer is the rate-limiting step, then j_{ph}~I_0.

It is indeed observed that for all measured photoanodes that the photocurrent grows linearly from 5 mW·cm^{-2} to 30 mW·cm^{-2} for all films (Figure 9a). The unmodified WO_3 film generates the lowest photocurrents, which is also proven by results presented in Figure 7, whereas the heterostructures show improved PEC activity at all light intensities. IPCE, on the other hand, is inversely related to I_0, which means that photon conversion efficiency drops with increasing light intensity. This trend is observed for the measured photoanodes (Figure 9b), wherein the largest IPCE values are calculated at 5 mW·cm^{-2}, and the lowest at 30 mW·cm^{-2}. The best photon conversion efficiency at 1.53 V was obtained for the 5-min-WO_3/MoS_x film, at 6%. It is also evident that after reduction, the r-30-min-WO_3/MoS_x photoanode's PEC properties improved significantly. The decrease in IPCE with I_0 is not as sharp for this film, which is a contrasting characteristic in comparison to the non-reduced films, in which IPCE drops with I_0 at a similar rate. The cause of this behavior is uncertain, but in practical terms, it means that higher light intensities can be used with fewer potential photon conversion efficiency losses.

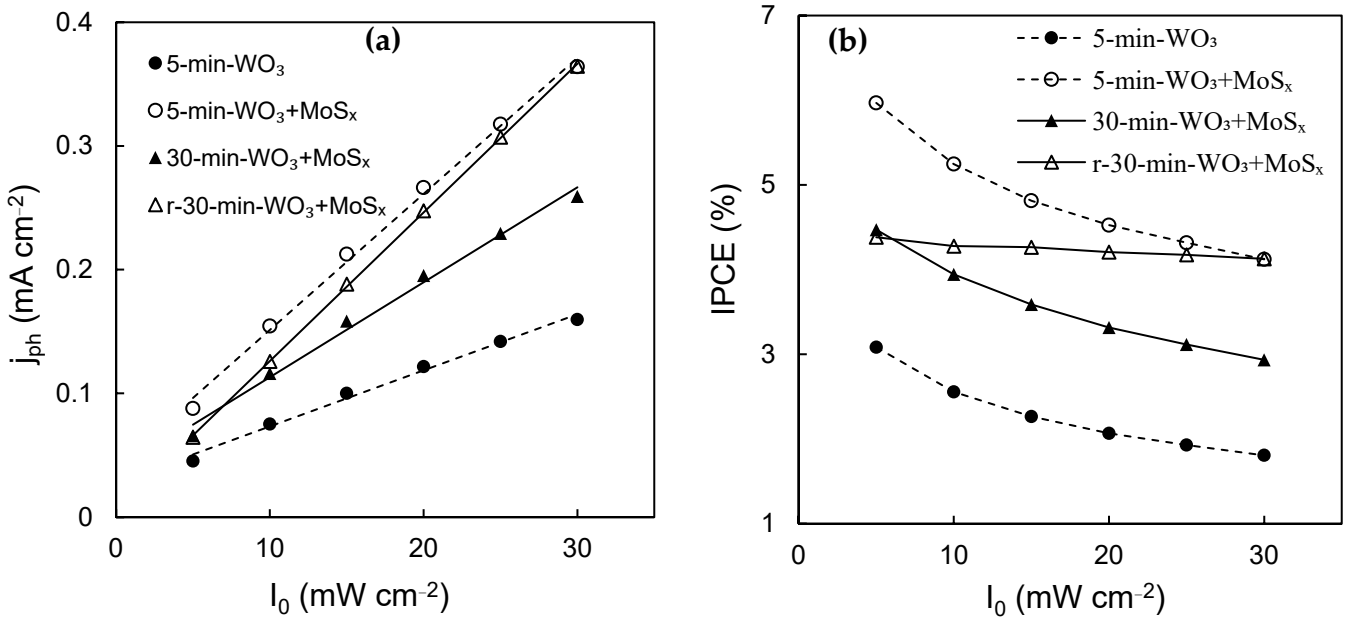

Figure 9. Values of photocurrents generated by WO_3, WO_3/MoS_x, and reduced WO_3/MoS_x films at 1.53 V and under different light intensities (**a**); IPCE (%) values calculated from photocurrents (**b**).

3.2.3. Scanning Electrochemical Microscopy of HER

Electrochemically deposited MoS_2 is typically an excellent HER catalyst in acidic media. MoS_{2-x} can be electrodeposited either cathodically or anodically (see Equation (7)). However, during PEO, MoS_x is incorporated into the oxide film through plasma discharges, as discussed in Section 3.1. XPS has already shown that stoichiometric MoS_2 exists on the surface of the heterostructured films. It was therefore decided to characterize their local and total HER electrocatalytic properties.

Due to the random nature of plasma discharges in PEO, MoS_x should not coat the anode surface evenly. Previous experience has shown that scanning electrochemical microscopy (SECM) can be used to measure the local hydrogen evolution activity of MoS_2 on complex surface structures [62]. The substrate generation–tip collection (SG-TC) mode is used, wherein the substrate generates hydrogen by the Heyrovsky step (Equation (8)) and the probe oxidizes it (Equation (9)):

$$\text{M–H} + H_3O^+ + e^- \rightleftarrows H_2 + H_2O + M \tag{8}$$

$$H_2 \rightarrow 2H^+ + 2e^- \tag{9}$$

It was determined that mild galvanostatic conditions are ideal for substrate generation. At -0.3 mA·cm^{-2}, the substrate emits a constant signal, and little gaseous hydrogen is produced. Because at cathodic potentials, WO_3/MoS_x not only generates H_2 but also intercalates H^+, the substrates were initially subjected to simple equilibration conditioning at -0.3 mA·cm^{-2} for 1200 s.

Additionally, it was important to relate the current measured by the probe to the signal produced by the substrate. To accomplish this, the probe current (i_{probe}) was recorded for 100 s with the substrate at OCP (Figure 10). After 100 s, a current of -0.3 mA was applied on the WO_3/MoS_x substrate, as previously, which caused the potential of the substrate to drop and settle at ~-0.42 V vs. sat Ag/AgCl within 120 s. During this time, i_{probe} rose rapidly to ~0.4 nA, which confirms that the probe does indeed react to the signal produced by the substrate. It must also be noted that i_{probe} is not particularly stable. Several sharp drops are seen, which were most likely caused by the accumulation of gaseous H_2 to form bubbles and block the probe. However, these conditions were considered optimal

for 2D mapping, and it was presumed that as the probe is mobile during a scan bubble, accumulation would be less likely.

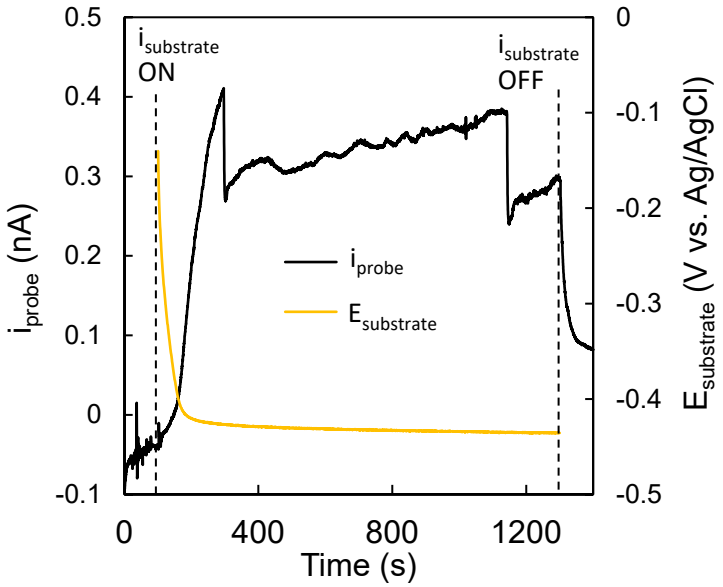

Figure 10. Trends of substrate potential and probe current over time. Obtained in 0.5 M H_2SO_4. Substrate, 5-min-WO_3/MoS_x; tip, 25 µm diameter Pt microelectrode.

The SECM mapping data are shown in Figure 11, which consists of 2D slices, as well as 2D and maps of the respective film. For 2-min-WO_3/MoS_x, no particularly features could be distinguished (Figure 11a–c). As expected from SEM and FIB observations, this seems to be the smoothest film in terms of surface roughnessand it contains the smallest amount of MoS_x. Even so, in the 2D profile, small bumps of current are observed at ~0.4–0.5 mm and 0.7 to 0.9 mm, but due to their linear continuity across the Y axis, these are more likely substrate topography-related signals. More interestingly, HER electrocatalytic activity maps are obtained for 5-min-WO_3/MoS_x (Figure 11d–f). In this case, significant inhomogeneity of HER activity is observed in the 1 × 1 mm map. Several islands of increased local activity emerge and occupy an area of ~0.2 × 0.2 mm. The 2D slices also show a more random distribution of HER activity compared to the previous film. This result certainly shows that areas of increased local HER activity exist on the surface of a WO_3/MoS_x heterostructure, but this may be related both to the presence of MoS_x as well as to the surface topography. Similar results were obtained for the 30-min-WO_3/MoS_x film (Figure 11g,h,j), showing comparable dimension spots of increased electrocatalytic activity on the surface. In this case, however, the difference between the smallest and largest measured currents is ~0.5 nA (for the 5-min-WO_3/MoS_x film it was 0.1 nA). If these results are cross-referenced with SEM and FIB observations, it may be inferred that this film, due to its larger roughness and MoS_x content, also has more inhomogeneity in local HER activity.

3.2.4. Total HER Activity

The HER electrocatalytic properties were also evaluated in terms of total electrode activity. The LSV curves shown in Figure 12a are corrected for iR-drop by the values of uncompensated resistance (often relating only to the resistance of the solution) obtained by means of EIS. These curves are typical of hydrogen's evolution in acidic media. All plain WO_3 films showed identical HER activity regardless of synthesis duration. The same is also true of the heterostructures, except for the 2-min-WO_3/MoS_x film, which could be expected due to its comparatively low MoS_x content. Therefore, a comparison is drawn between a characteristic WO_3 and a 5-min-WO_3/MoS_x film. The WO_3 film has an η_{10mA} (overpotential at which 10 mA·cm^{-2} HER current is reached) of −0.45 V, and a Tafel slope of 74.1 mA·dec^{-1}. The comparable WO_3/MoS_x exhibits significantly better electrocatalytic

activity, having a η_{10mA} of −0.22 V and a Tafel slope of 42.6 mV·dec^{-1}. Both parameters are ~2 times better in terms of efficiency in comparison to the respective WO_3 films, and are typical of MoS_2-based materials in acidic media [25].

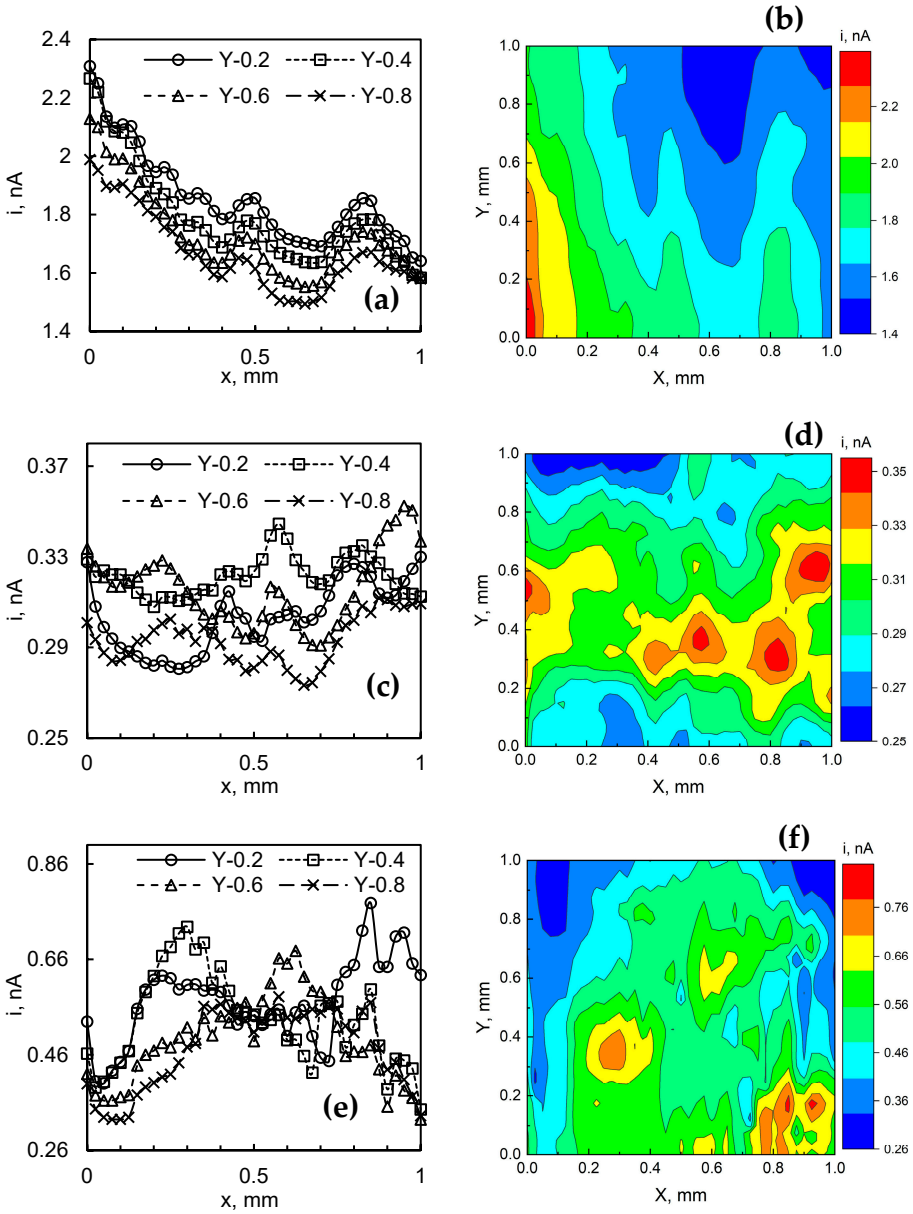

Figure 11. 2D profiles and 2D SECM maps: 2-min-WO_3/MoS_x (**a**,**b**); 5-min-WO_3/MoS_x (**c**,**d**); 30-min-WO_3/MoS_x (**e**,**f**) films, obtained in 0.5 M H_2SO_4. Probe scan speed 100 μm s^{-1}, data acquisition at 25 μm intervals with a 25 μm diameter probe.

In addition, EIS was used to characterize the catalyst–solution interface at increasing overpotentials. When comparing WO_3 and heterostructured films at the same overpotential, it is apparent that the impedance of the WO_3/MoS_x film is smaller (Figure 12b) because the rate of HER is higher. Here, the spectrum in the Nyquist coordinates is represented by a low-frequency semicircle, which is related to the rate-limiting hydrogen adsorption process for HER on MoS_2 under such conditions [24].

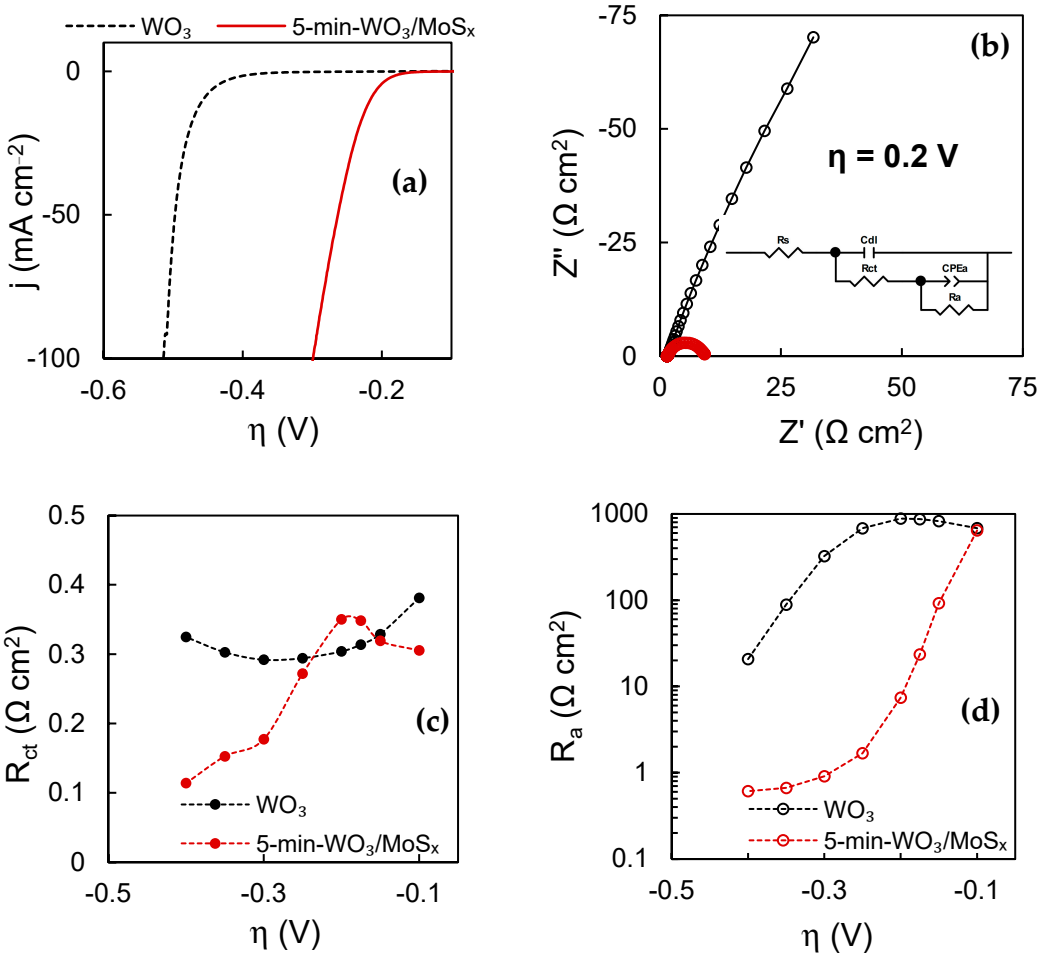

Figure 12. HER characterization data of WO_3 and heterostructured films: LSV scans at 2 mV s^{-1} corrected by iR-drop (**a**); EIS spectra obtained at overpotential −0.2 V in complex plane coordinates, where solid lines show equivalent circuit fits (inset shows equivalent circuit used to fit spectra) (**b**); values of R_{ct} as a function of overpotential (**c**); values of R_a as a function of overpotential (**d**).

By fitting the obtained impedance spectra to an equivalent electric circuit (EEC), the values of the discrete capacitive and resistive features of the catalyst–solution interface can be calculated. The used circuit is shown in the inset of Figure 12b, where R_s is the uncompensated resistance (solution resistance), C_{dl} is the double layer capacitance, R_{ct} is the charge transfer resistance, CPE_a is the constant phase element that models hydrogen adsorption related capacitance, and R_a is the hydrogen adsorption resistance.

This model comprises two RC components: the high frequency component (C_{dl}-R_{ct}) that is related to the Heyrovsky electrochemical recombination step, and the low frequency component (CPE_a-R_a) that simulates the slower Volmer hydrogen adsorption step. The resistance parameters are inversely related to the rate of their corresponding electrochemical reactions, and therefore their relation to the applied overpotential gives information on the kinetics of the hydrogen evolution reaction. For both WO_3 and WO_3/MoS_x, R_{ct} values (Figure 12c) are similar in the overpotential range, where little HER occurs (−0.1 V to ~−0.2 V). However, for WO_3/MoS_x, R_{ct} drops sharply from ~−0.2 V, coinciding with the onset of vigorous HER. At −0.4 V, R_{ct} approaches the lowest value of 0.11 Ω cm^2. The WO_3 film does not exhibit this behavior because the HER current density at −0.4 V was only approximately 1.5 mA·cm^{-2}. Moreover, C_{dl} is caused by the charge/discharge of the double layer at the catalyst–solution interface, and is therefore proportional to the electrochemically active surface area (ECSA). It was found that C_{dl} values obtained at −0.1 V for the 2-min, 5 min and 30 min films were 0.73 mF·cm^{-2}, 1.06 mF·cm^{-2} and

1.53 mF·cm^{-2}, respectively, showing that longer synthesis durations resulted in a larger ECSA. The same ratio was retained at each applied overpotential. For comparison, C_{dl} of the 5-min-WO_3 film was 1.17 mF·cm^{-2}, which shows that the non-heterostructured film has a slightly larger electrochemically active surface area.

The hydrogen adsorption resistance R_a is even more closely linked to the HER activity of the catalysts. Because the rate of HER is limited by the Volmer hydrogen adsorption step, the measured current density and overall reaction rate are determined by the low-frequency adsorption-related parameters, especially R_a. The adsorption resistance decreases with increasingly negative overpotentials because H^+ is more readily adsorbed (Figure 12d). However, it is apparent that on the heterostructured material, R_a drops more swiftly until ~−0.3 V and then plateaus. For WO_3, in contrast, R_a continues to decrease at −0.4 V. Experiments showed that at large enough overpotentials, the R_a values become equal, but for the heterostructure, lower R_a values are reached at lower overpotentials, which is expected of a heterogeneous HER electrocatalyst.

4. Conclusions

In this work, a bifunctional catalyst based on WO_3 and MoS_2 was prepared by relatively low-current plasma electrolytic oxidation of W in an electrolyte containing a MoS_4^{2-} precursor. SEM observations revealed a rough surface morphology comprising disordered pores of up to 500 nm diameter, depending on synthesis time. Film thickness was also directly related to the duration of synthesis, and ranged from 0.56 µm to 3.5 µm. The presence of non-stoichiometric MoS_x was confirmed by EDX and observed by elemental mapping only for the thickest film. XPS measurements showed a relatively strong Mo^{4+}-S signal, suggesting that stoichiometric MoS_2 also exists in the film. Although the films were not annealed, due to the nature of PEO, they exhibited a degree of crystallinity, and the WO_3 was found to be monoclinic. The band gap ranged from 2.38 eV to 2.75 eV, depending on the duration of synthesis. This crystallinity and the incorporation of a lower band gap material (MoS_2) means that even the as-deposited films performed as rather efficient photoanodes for photoelectrochemical water splitting, and could reach an IPCE of ~6%. The effect of electrochemical reduction was also discussed and used to further improve the PEC activity. Due to the presence of MoS_x these materials can also act as HER electrocatalysts, and this was confirmed by measuring their HER activity in 0.5 M H_2SO_4. The best obtained Tafel slope (42.6 mV·dec^{-1}) can be compared to that of electrocatalytic MoS_2 films. Electrochemical impedance spectroscopy confirmed that the improved electrocatalytic HER activity is due to enhanced H^+ adsorption, which is attributed to MoS_2. Scanning electrochemical microscopy was used to evaluate the local HER activity of the heterostructured films. It was found that differences in local activity can be discerned on a millimeter-level and could be related to the synthesis duration of the respective films (and thus to morphology and composition). Overall, the WO_3/MoS_x heterostructures combine the best photo/electrochemical properties of WO_3 and MoS_2 into one versatile smart material.

Author Contributions: Conceptualization, R.L., N.T. and H.C.; methodology, R.L. and N.T.; formal analysis, R.L.; investigation, R.L., R.V. and K.G.; resources, H.C., R.V., L.T.-T. and E.N.; writing—original draft preparation, R.L.; writing—review and editing, R.L., N.T., H.C., L.T.-T. and E.N.; visualization, R.L., R.V. and K.G.; supervision, H.C. and E.N.; project administration, H.C.; funding acquisition, H.C. All authors have read and agreed to the published version of the manuscript.

Funding: This research has received funding from the European Union's Horizon 2020 research and innovation program under the Marie Sklodowska-Curie grant agreement, No. 778357-SMARTELECTRODES. It has been performed in cooperation with the Research Council of Lithuania (LMTLT), agreement No. S-PD-22-5—TICAL, and partially with National Agency for Research and Development, Moldova, project No. 20.80009.5007.18.

Institutional Review Board Statement: Not applicable.

Informed Consent Statement: Not applicable.

Data Availability Statement: Data sharing is not applicable to this article.

Conflicts of Interest: The authors declare no conflict of interest.

References

1. Xu, S.; Carter, E.A. Theoretical Insights into Heterogeneous (Photo)Electrochemical CO_2 Reduction. *Chem. Rev.* **2019**, *119*, 6631–6669. [CrossRef] [PubMed]
2. Gopinath, M.; Marimuthu, R. A Review on Solar Energy-Based Indirect Water-Splitting Methods for Hydrogen Generation. *Int. J. Hydrogen Energy* **2022**, *47*, 37742–37759. [CrossRef]
3. Møller, K.T.; Jensen, T.R.; Akiba, E.; Li, H. Hydrogen—A Sustainable Energy Carrier. *Prog. Nat. Sci. Mater. Int.* **2017**, *27*, 34–40. [CrossRef]
4. Wappler, M.; Unguder, D.; Lu, X.; Ohlmeyer, H.; Teschke, H.; Lueke, W. Building the Green Hydrogen Market—Current State and Outlook on Green Hydrogen Demand and Electrolyzer Manufacturing. *Int. J. Hydrogen Energy* **2022**, *47*, 33551–33570. [CrossRef]
5. Razi, F.; Dincer, I. A Critical Evaluation of Potential Routes of Solar Hydrogen Production for Sustainable Development. *J. Clean. Prod.* **2020**, *264*, 121582. [CrossRef]
6. Morales, W.; Cason, M.; Aina, O.; de Tacconi, N.R.; Rajeshwar, K. Combustion Synthesis and Characterization of Nanocrystalline WO_3. *J. Am. Chem. Soc.* **2008**, *130*, 6318–6319. [CrossRef]
7. Widiyandari, H.; Firdaus, I.; Kadarisman, V.G.S.; Purwanto, A. Optical Properties and Photocatalytic Activities of Tungsten Oxide (WO_3) with Platinum Co-Catalyst Addition. In *AIP Conference Proceedings*; AIP Publishing LLC: Jatinangor, Indonesia, 2016; p. 050027.
8. Bharagav, U.; Ramesh Reddy, N.; Nava Koteswara Rao, V.; Ravi, P.; Sathish, M.; Rangappa, D.; Prathap, K.; Shilpa Chakra, C.; Shankar, M.V.; Appels, L.; et al. Bifunctional G-C3N4/Carbon Nanotubes/WO_3 Ternary Nanohybrids for Photocatalytic Energy and Environmental Applications. *Chemosphere* **2023**, *311*, 137030. [CrossRef] [PubMed]
9. Knöppel, J.; Kormányos, A.; Mayerhöfer, B.; Hofer, A.; Bierling, M.; Bachmann, J.; Thiele, S.; Cherevko, S. Photocorrosion of WO_3 Photoanodes in Different Electrolytes. *ACS Phys. Chem. Au* **2021**, *1*, 6–13. [CrossRef] [PubMed]
10. Bai, S.; Zhang, K.; Luo, R.; Li, D.; Chen, A.; Liu, C.C. Low-Temperature Hydrothermal Synthesis of WO_3 Nanorods and Their Sensing Properties for NO_2. *J. Mater. Chem.* **2012**, *22*, 12643. [CrossRef]
11. Tehrani, F.S.; Ahmadian, H.; Aliannezhadi, M. Hydrothermal Synthesis and Characterization of WO_3 Nanostructures: Effect of Reaction Time. *Mater. Res. Express* **2020**, *7*, 015911. [CrossRef]
12. Judeinstein, P.; Livage, J. Sol–Gel Synthesis of WO_3 Thin Films. *J. Mater. Chem.* **1991**, *1*, 621–627. [CrossRef]
13. Mohamedkhair, A.K.; Drmosh, Q.A.; Qamar, M.; Yamani, Z.H. Tuning Structural Properties of WO_3 Thin Films for Photoelectrocatalytic Water Oxidation. *Catalysts* **2021**, *11*, 381. [CrossRef]
14. Sadale, S.B.; Chaqour, S.M.; Gorochov, O.; Neumann-Spallart, M. Photoelectrochemical and Physical Properties of Tungsten Trioxide Films Obtained by Aerosol Pyrolysis. *Mater. Res. Bull.* **2008**, *43*, 1472–1479. [CrossRef]
15. Brada, M.; Neumann-Spallart, M.; Krýsa, J. Tungsten Trioxide Film Photoanodes Prepared by Aerosol Pyrolysis for Photoelectrochemical Applications. *Catal. Today* **2022**, *413–415*, 113981. [CrossRef]
16. Poongodi, S.; Kumar, P.S.; Mangalaraj, D.; Ponpandian, N.; Meena, P.; Masuda, Y.; Lee, C. Electrodeposition of WO_3 Nanostructured Thin Films for Electrochromic and H_2S Gas Sensor Applications. *J. Alloys Compd.* **2017**, *719*, 71–81. [CrossRef]
17. Mineo, G.; Ruffino, F.; Mirabella, S.; Bruno, E. Investigation of WO_3 Electrodeposition Leading to Nanostructured Thin Films. *Nanomaterials* **2020**, *10*, 1493. [CrossRef]
18. Coelho, D.; Gaudêncio, J.P.R.S.; Carminati, S.A.; Ribeiro, F.W.P.; Nogueira, A.F.; Mascaro, L.H. Bi Electrodeposition on WO_3 Photoanode to Improve the Photoactivity of the $WO_3/BiVO_4$ Heterostructure to Water Splitting. *Chem. Eng. J.* **2020**, *399*, 125836. [CrossRef]
19. Levinas, R.; Tsyntsaru, N.; Lelis, M.; Cesiulis, H. Synthesis, Electrochemical Impedance Spectroscopy Study and Photoelectrochemical Behaviour of as-Deposited and Annealed WO_3 Films. *Electrochim. Acta* **2017**, *225*, 29–38. [CrossRef]
20. Fernández-Domene, R.M.; Roselló-Márquez, G.; Sánchez-Tovar, R.; Cifre-Herrando, M.; García-Antón, J. Synthesis of WO_3 Nanorods through Anodization in the Presence of Citric Acid: Formation Mechanism, Properties and Photoelectrocatalytic Performance. *Surf. Coat. Technol.* **2021**, *422*, 127489. [CrossRef]
21. Yeh, C.-W.; Wu, K.-R.; Hung, C.-H.; Chang, H.-C.; Hsu, C.-J. Preparation of Porous F-WO_3/TiO_2 Films with Visible-Light Photocatalytic Activity by Microarc Oxidation. *Int. J. Photoenergy* **2012**, *2012*, 285129. [CrossRef]
22. Stojadinović, S.; Radić, N.; Vasilić, R.; Petković, M.; Stefanov, P.; Zeković, L.; Grbić, B. Photocatalytic Properties of TiO_2/WO_3 Coatings Formed by Plasma Electrolytic Oxidation of Titanium in 12-Tungstosilicic Acid. *Appl. Catal. B Environ.* **2012**, *126*, 334–341. [CrossRef]
23. Bayati, M.R.; Golestani-Fard, F.; Moshfegh, A.Z.; Molaei, R. A Photocatalytic Approach in Micro Arc Oxidation of WO_3–TiO_2 Nano Porous Semiconductors under Pulse Current. *Mater. Chem. Phys.* **2011**, *128*, 427–432. [CrossRef]
24. Meng, C.; Chen, X.; Gao, Y.; Zhao, Q.; Kong, D.; Lin, M.; Chen, X.; Li, Y.; Zhou, Y. Recent Modification Strategies of MoS_2 for Enhanced Electrocatalytic Hydrogen Evolution. *Molecules* **2020**, *25*, 1136. [CrossRef] [PubMed]
25. Benck, J.D.; Hellstern, T.R.; Kibsgaard, J.; Chakthranont, P.; Jaramillo, T.F. Catalyzing the Hydrogen Evolution Reaction (HER) with Molybdenum Sulfide Nanomaterials. *ACS Catal.* **2014**, *4*, 3957–3971. [CrossRef]

26. Seo, B.; Joo, S.H. Recent Advances in Unveiling Active Sites in Molybdenum Sulfide-Based Electrocatalysts for the Hydrogen Evolution Reaction. *Nano Converg.* **2017**, *4*, 19. [CrossRef] [PubMed]
27. Tang, Q.; Jiang, D. Stabilization and Band-Gap Tuning of the 1T-MoS_2 Monolayer by Covalent Functionalization. *Chem. Mater.* **2015**, *27*, 3743–3748. [CrossRef]
28. Zhu, Y.; Song, L.; Song, N.; Li, M.; Wang, C.; Lu, X. Bifunctional and Efficient CoS_2–C@MoS_2 Core–Shell Nanofiber Electrocatalyst for Water Splitting. *ACS Sustain. Chem. Eng.* **2019**, *7*, 2899–2905. [CrossRef]
29. Ali, S.A.; Ahmad, T. Chemical Strategies in Molybdenum Based Chalcogenides Nanostructures for Photocatalysis. *Int. J. Hydrogen Energy* **2022**, *47*, 29255–29283. [CrossRef]
30. Zhou, D.; Shu, H.; Hu, C.; Jiang, L.; Liang, P.; Chen, X. Unveiling the Growth Mechanism of MoS_2 with Chemical Vapor Deposition: From Two-Dimensional Planar Nucleation to Self-Seeding Nucleation. *Cryst. Growth Des.* **2018**, *18*, 1012–1019. [CrossRef]
31. Cho, Y.J.; Sim, Y.; Lee, J.-H.; Hoang, N.T.; Seong, M.-J. Size and Shape Control of CVD-Grown Monolayer MoS_2. *Curr. Appl. Phys.* **2023**, *45*, 99–104. [CrossRef]
32. Yue, J.; Jian, J.; Dong, P.; Luo, L.; Chang, F. Growth of Single-Layer MoS_2 by Chemical Vapor Deposition on Sapphire Substrate. *IOP Conf. Ser. Mater. Sci. Eng.* **2019**, *592*, 012044. [CrossRef]
33. Vattikuti, S.V.P.; Byon, C.; Reddy, C.V. Synthesis of MoS_2 Multi-Wall Nanotubes Using Wet Chemical Method with H_2O_2 as Growth Promoter. *Superlattices Microstruct.* **2015**, *85*, 124–132. [CrossRef]
34. Wojtalik, M.; Bojarska, Z.; Makowski, Ł. Experimental Studies on the Chemical Wet Synthesis for Obtaining High-Quality MoS_2 Nanoparticles Using Impinging Jet Reactor. *J. Solid State Chem.* **2020**, *285*, 121254. [CrossRef]
35. Falola, B.D.; Wiltowski, T.; Suni, I.I. Electrodeposition of MoS_2 for Charge Storage in Electrochemical Supercapacitors. *J. Electrochem. Soc.* **2016**, *163*, D568–D574. [CrossRef]
36. Levinas, R.; Tsyntsaru, N.; Cesiulis, H. Insights into Electrodeposition and Catalytic Activity of MoS_2 for Hydrogen Evolution Reaction Electrocatalysis. *Electrochim. Acta* **2019**, *317*, 427–436. [CrossRef]
37. Noori, Y.J.; Thomas, S.; Ramadan, S.; Smith, D.E.; Greenacre, V.K.; Abdelazim, N.; Han, Y.; Beanland, R.; Hector, A.L.; Klein, N.; et al. Large-Area Electrodeposition of Few-Layer MoS_2 on Graphene for 2D Material Heterostructures. *ACS Appl. Mater. Interfaces* **2020**, *12*, 49786–49794. [CrossRef]
38. Vizza, M.; Giurlani, W.; Cerri, L.; Calisi, N.; Leonardi, A.A.; Faro, M.J.L.; Irrera, A.; Berretti, E.; Perales-Rondón, J.V.; Colina, A.; et al. Electrodeposition of Molybdenum Disulfide (MoS_2) Nanoparticles on Monocrystalline Silicon. *Molecules* **2022**, *27*, 5416. [CrossRef]
39. Rakibuddin, M.; Kim, H. Fabrication of MoS_2 /WO_3 Nanocomposite Films for Enhanced Electro-Chromic Performance. *New J. Chem.* **2017**, *41*, 15327–15333. [CrossRef]
40. Singh, S.; Sharma, S. Ammonia Sensing Using MoS_2/WO_3 Composite Obtained via Top-down Approach. *Mater. Today Proc.* **2021**, *43*, 137–140. [CrossRef]
41. Shahid, W.; Idrees, F.; Iqbal, M.A.; Tariq, M.U.; Shahid, S.; Choi, J.R. Ex Situ Synthesis and Characterizations of MoS_2/WO_3 Heterostructures for Efficient Photocatalytic Degradation of RhB. *Nanomaterials* **2022**, *12*, 2974. [CrossRef]
42. Simchen, F.; Sieber, M.; Kopp, A.; Lampke, T. Introduction to Plasma Electrolytic Oxidation—An Overview of the Process and Applications. *Coatings* **2020**, *10*, 628. [CrossRef]
43. Sikdar, S.; Menezes, P.V.; Maccione, R.; Jacob, T.; Menezes, P.L. Plasma Electrolytic Oxidation (PEO) Process—Processing, Properties, and Applications. *Nanomaterials* **2021**, *11*, 1375. [CrossRef] [PubMed]
44. Levinas, R.; Tsyntsaru, N.; Cesiulis, H. The Characterisation of Electrodeposited MoS_2 Thin Films on a Foam-Based Electrode for Hydrogen Evolution. *Catalysts* **2020**, *10*, 1182. [CrossRef]
45. Levinas, R.; Tsyntsaru, N.; Murauskas, T.; Cesiulis, H. Improved Photocatalytic Water Splitting Activity of Highly Porous WO_3 Photoanodes by Electrochemical H+ Intercalation. *Front. Chem. Eng.* **2021**, *3*, 760700. [CrossRef]
46. Mortazavi, G.; Jiang, J.; Meletis, E.I. Investigation of the Plasma Electrolytic Oxidation Mechanism of Titanium. *Appl. Surf. Sci.* **2019**, *488*, 370–382. [CrossRef]
47. Venkateswarlu, K.; Rameshbabu, N.; Sreekanth, D.; Sandhyarani, M.; Bose, A.C.; Muthupandi, V.; Subramanian, S. Role of Electrolyte Chemistry on Electronic and in Vitro Electrochemical Properties of Micro-Arc Oxidized Titania Films on Cp Ti. *Electrochim. Acta* **2013**, *105*, 468–480. [CrossRef]
48. Qi, H.; Wolfe, J.; Wang, D.; Fan, H.J.; Fichou, D.; Chen, Z. Triple-Layered Nanostructured WO_3 Photoanodes with Enhanced Photocurrent Generation and Superior Stability for Photoelectrochemical Solar Energy Conversion. *Nanoscale* **2014**, *6*, 13457–13462. [CrossRef]
49. Polunin, A.V.; Cheretaeva, A.O.; Borgardt, E.D.; Rastegaev, I.A.; Krishtal, M.M.; Katsman, A.V.; Yasnikov, I.S. Improvement of Oxide Layers Formed by Plasma Electrolytic Oxidation on Cast Al Si Alloy by Incorporating TiC Nanoparticles. *Surf. Coat. Technol.* **2021**, *423*, 127603. [CrossRef]
50. Bhattacharya, R.N.; Lee, C.Y.; Pollak, F.H.; Schleich, D.M. Optical Study of Amorphous MoS3: Determination of the Fundamental Energy Gap. *J. Non-Cryst. Solids* **1987**, *91*, 235–242. [CrossRef]
51. Laperriere, G.; Marsan, B.; Belanger, D. Preparation and Characterization of Electrodeposited Amorphous Molybdenum Sulfide. *Synth. Met.* **1989**, *29*, 201–206. [CrossRef]

52. Bélanger, D.; Laperriére, G.; Marsan, B. The Electrodeposition of Amorphous Molybdenum Sulfide. *J. Electroanal. Chem.* **1993**, *347*, 165–183. [CrossRef]
53. Ismail, S.; Ng, C.Y.; Ahmadi, E.; Razak, K.A.; Lockman, Z. Segmented Nanoporous WO_3 Prepared via Anodization and Their Photocatalytic Properties. *J. Mater. Res.* **2016**, *31*, 721–728. [CrossRef]
54. Chen, J.; Xia, Y.; Yang, J.; Chen, B. Fabrication of Monolayer MoS_2/RGO Hybrids with Excellent Tribological Performances through a Surfactant-Assisted Hydrothermal Route. *Appl. Phys. A* **2018**, *124*, 430. [CrossRef]
55. Li, Y.; Nakamura, R. Structural Change of Molybdenum Sulfide Facilitates the Electrocatalytic Hydrogen Evolution Reaction at Neutral PH as Revealed by in Situ Raman Spectroscopy. *Chin. J. Catal.* **2018**, *39*, 401–406. [CrossRef]
56. Kibsgaard, J.; Jaramillo, T.F.; Besenbacher, F. Building an Appropriate Active-Site Motif into a Hydrogen-Evolution Catalyst with Thiomolybdate [Mo3S13]2− Clusters. *Nat. Chem* **2014**, *6*, 248–253. [CrossRef] [PubMed]
57. Tran, P.D.; Tran, T.V.; Orio, M.; Torelli, S.; Truong, Q.D.; Nayuki, K.; Sasaki, Y.; Chiam, S.Y.; Yi, R.; Honma, I.; et al. Coordination Polymer Structure and Revisited Hydrogen Evolution Catalytic Mechanism for Amorphous Molybdenum Sulfide. *Nat. Mater* **2016**, *15*, 640–646. [CrossRef]
58. Merki, D.; Fierro, S.; Vrubel, H.; Hu, X. Amorphous Molybdenum Sulfide Films as Catalysts for Electrochemical Hydrogen Production in Water. *Chem. Sci.* **2011**, *2*, 1262–1267. [CrossRef]
59. Abe, R.; Takami, H.; Murakami, N.; Ohtani, B. Pristine Simple Oxides as Visible Light Driven Photocatalysts: Highly Efficient Decomposition of Organic Compounds over Platinum-Loaded Tungsten Oxide. *J. Am. Chem. Soc.* **2008**, *130*, 7780–7781. [CrossRef]
60. Boruah, P.J.; Khanikar, R.R.; Bailung, H. Synthesis and Characterization of Oxygen Vacancy Induced Narrow Bandgap Tungsten Oxide (WO_{3-x}) Nanoparticles by Plasma Discharge in Liquid and Its Photocatalytic Activity. *Plasma Chem Plasma Process* **2020**, *40*, 1019–1036. [CrossRef]
61. Hankin, A.; Bedoya-Lora, F.E.; Alexander, J.C.; Regoutz, A.; Kelsall, G.H. Flat Band Potential Determination: Avoiding the Pitfalls. *J. Mater. Chem. A* **2019**, *7*, 26162–26176. [CrossRef]
62. Levinas, R.; Grigucevičienė, A.; Kubilius, T.; Matijošius, A.; Tamašauskaitė-Tamašiūnaitė, L.; Cesiulis, H.; Norkus, E. Femtosecond Laser-Ablated Copper Surface as a Substrate for a MoS_2-Based Hydrogen Evolution Reaction Electrocatalyst. *Materials* **2022**, *15*, 3926. [CrossRef] [PubMed]